Parametrically Driven Inertial Sensing in Chip-Scale Optomechanical Cavities at the Thermodynamical Limits with Extended Dynamic Range

Jaime Gonzalo Flor Flores,* Talha Yerebakan, Wenting Wang, Mingbin Yu, Dim-Lee Kwong, Andrey Matsko, and Chee Wei Wong*

Recent scientific and technological advances have enabled the detection of gravitational waves, autonomous driving, and the proposal of a communications network on the Moon (Lunar Internet or LunaNet). These efforts are based on the measurement of minute displacements and their corresponding force transduction, which enables acceleration, velocity, and position determination for navigation. State-of-the-art accelerometers use capacitive or piezoresistive techniques and micro-electromechanical systems (MEMS) via integrated circuit (IC) technologies to drive transducers and convert their output for electric readout. In recent years, laser optomechanical transduction and readout have enabled highly sensitive detection of motional displacement. Here the theoretical framework is further examined for the novel mechanical frequency readout technique of optomechanical transduction when the sensor is driven into oscillation mode. Theoretical and physical agreements are demonstrated, and the most relevant performance parameters are characterized by a device with a 1.5 mg Hz^{-1} acceleration sensitivity, a 2.5 fm Hz$^{-1/2}$ displacement resolution corresponding to a 17.02 µg Hz$^{-1/2}$ force-equivalent acceleration, and a 5.91 Hz nW^{-1} power sensitivity, at the thermodynamical limits. In addition, a novel technique is presented for dynamic range extension while maintaining the precision sensing sensitivity. This inertial accelerometer is integrated on-chip and enabled for packaging, with a laser-detuning-enabled approach.

J. G. Flor Flores, T. Yerebakan, W. Wang, C. W. Wong
Fang Lu Mesoscopic Optics and Quantum Electronics Laboratory
University of California
Los Angeles, CA 90095, USA
E-mail: jflorflores@ucla.edu; cheewei.wong@ucla.edu
M. Yu, D.-L. Kwong
Institute of Microelectronics
A*STAR
Singapore 117865, Singapore
A. Matsko
Jet Propulsion Laboratory (JPL)
California Institute of Technology
Pasadena, CA 91109, USA

1. Introduction

In general, accelerometers use a sensing method based on Hooke's Law, where a proof mass is attached to a spring-like mechanism, and the applied acceleration introduces a perturbation that moves it away from a "zero-point" position. These accelerometers measure the displacement of the proof mass to infer the specific force applied to the system. For these accelerometers, the mechanical quality factor (Q_m), defined as a function of the damping ratio (ζ) as $Q_m = \frac{1}{2\zeta}$, should be engineered such that the transducer is able to dissipate the applied force fast enough to preserve the system's sensing bandwidth. For example, a transducer with a low mechanical quality factor Q_m of 5, equivalent to a damping ratio of 0.1, will have its oscillation amplitude reduced by ½ after only one oscillation cycle.[1–10] A large variety of commercial accelerometers in the market use this principle, including micro-electromechanical system (MEMS), capacitive and piezoelectric accelerometers. Instead, optomechanical accelerometers[11,12] use a variation of this principle, where displacement is measured in the mechanical domain and resonant cavity frequency shift is measured in the optical domain. At its core, displacement is measured through detection of changes in the cavity field from dispersive and dissipative effects that can alter the cavity's linewidth and modulate its power. The measurement noise can be determined through the power spectral density (PSD) by applying the Wiener–Khinchin theorem that relates it to the Fourier transform of the autocorrelation function of the noise. The mechanical resonator is configured to enhance the response to the external force since the resonant amplitude displacement is proportional to the energy in the resonator,[13,14] and reductions in the thermal noise floor lower the limit of the minimum detectable force.[15]

With a variation of the previously described principle, measurement of acceleration can also be achieved by detecting the change in resonant frequency of an oscillating transducer, such as the one driven by cavity optomechanics. In resonant MEMS accelerometers, such as vibrating beam accelerometers (VBA),

this is achieved by loading a proof mass to a beam oscillator or a double-ended tuning fork, which changes its mechanical frequency when subjected to inertial forces.[16,17] This type of accelerometer requires high Q_m as it needs a narrow linewidth to achieve high sensitivity. In addition, traditional resonant accelerometers require the appropriate driving and feedback mechanism suitable to accurately sustain the resonator's amplitude of oscillation, and prevent it from entering into a nonlinear region.

This feedback system usually requires an external circuit with multiple components such as a front-end amplifier, an amplitude detector, an error amplifier, a loop filter, and a variable gain amplifier.[18,19] Since thermal noise produces a contribution to phase noise that is proportional to $1/f^2$, it is important to take into account contributions from the feedback system, which can eventually dominate this decay and make the noise spectrum become flat at higher frequencies.[20–22] Therefore, the feedback loop needs to be carefully designed in such a way that its Brownian noise spectrum is smaller than that of the resonator. An example schematic MEMS resonant accelerometer with an integrated feedback system is illustrated in Section SI (Supporting Information). While these components are justified by the bias instability and noise density performance improvement of resonant accelerometers, an integrated physical system with feedback that exceeds the state-of-the-art figures of merit with low noise and size, which does not require a multitude of external components, is attractive to the community.

Our chip-scale cavity optomechanical inertial sensor, laser-driven parametrically and with intrinsic feedback, provides 1.5 mg Hz^{-1} sensitivity, 2.5 fm Hz$^{-1/2}$ displacement resolution (DR), with 5.91 Hz nW^{-1} power sensitivity, and 17.02 µg Hz$^{-1/2}$ force-equivalent acceleration close to the thermodynamical limits. Our transducer architecture does not measure specific force by direct displacement, as examined by prior optomechanical, optical interferometric, and other sensor studies.[11,12,23] Instead, it is based on resonant frequency transduction as described above. Furthermore, our platform depends neither on the measured force to generate compression–tension in the mechanical system (with subsequent changes in the resonant mechanical frequency) nor on a force rebalancing method. Our measurement principle is fundamentally based on the optomechanical optical-spring effect, through parametrically driven coupling between the optical and mechanical modes with intrinsic feedback. This enables the use of a small sensing mass that gathers less inertial force than a larger one, producing a smaller transduction displacement. This means that the device is not mechanically limited by risking entrance to the nonlinear displacement region. Taking advantage of the optical feedback system for increased noise reduction, the optomechanical transducer has spare mechanical range that enables dynamic range extension without sacrificing resolution, translating an apparent technological disadvantage into an advantage of this technology.

2. Optomechanical Inertial Accelerometer with RF Sensing Mechanism

2.1. System Description

Figure 1 illustrates the scanning electron microscopic (SEM) image of our optomechanical accelerometer which consists of a photonic crystal cavity (colored in orange) that is parametrically coupled to a mechanical resonant mode[8,24–26] with a side-attached large motional mass (colored in green). The yellow region is the stationary mass, anchored in the silicon device layer. The motional mass is free to oscillate in the x-direction, with an oscillation frequency in the radio frequency (RF) range, mainly given by four cantilever beams used for suspension. In addition, the device features integrated waveguides, marked in purple on the figure, which couple the driving laser to the photonic crystal and the output detector. The waveguides extend across the chiplet and have an inverse tapered coupler on each side. These waveguides provide less input/output power loss and mechanical noise compared to previous methods that use a dimpled tapered fiber to couple from the top of the device. Moreover, the use of these waveguides constitutes an important step toward system integration and enables the enclosure of the chiplet on a hermetic butterfly package.

The optical cavity is designed and implemented inside a 2D photonic crystal slab of the *p6m* hexagonal symmetry group, with a center singular row of lattice holes removed and replaced by an air-slot waveguide in the propagation *y*-axis. The optical mode has strong in-plane *xy* transverse confinement due to the large index contrast in the photonic crystal. The slot width is $s = 100$ nm, and the hole array has a lattice constant of $a_p = 510$ nm and a radius of $r = 185$ nm. To form an optical resonant cavity in the slot waveguide, three nearest rows of holes next to the slot are lattice perturbed by 5, 10, and 15 nm, respectively,[27] as shown in Section SII (Supporting Information). The cavity has a subwavelength $0.051(\lambda/n)^3$ mode volume V_m. The lattice perturbations are designed to preserve the mode confinement while achieving a good quality factor Q for a high Q/V ratio.[28,29] The measured cavity transmissions for different input powers are shown in Figure 1b.

2.2. Optomechanical Transduction

The core of the optomechanical accelerometer lies in the subwavelength slot photonic crystal cavity, designed to have a resonant optical frequency at 1559.75 nm, as shown in Figure 1b. With the cavity driven by the pump laser, the circulating photons impart an optical gradient force in the subwavelength slot, with the in-plane x-direction optomechanical force onto the cavity walls. The optical gradient force displaces the motional mass, increasing the slot cavity width, and detuning the optical resonance from the pump. This subsequently lowers the cavity electromagnetic intensity, reducing the optical gradient force, which decreases the width of the slot cavity again. Once the cavity slot width is reduced, the process repeats, allowing the optomechanical cavity to sustain periodical motion (gain) with regenerative oscillations.[30–33] The parametric process just described represents an intrinsic optical feedback system that drives the cavity and does not need the external electrical components required by the techniques described in the previous section.

The optomechanical transduction described is given by the co-design of the optical cavity mode i, the W1 line defect, and the fundamental in-plane mechanical mode, as shown in **Figure 2**a. This interaction is described by the shift in optical frequency ω_o due to a shift in the motional mass displacement or equivalently $d\omega_o/dx$, and is defined as the optomechanical coupling

ADVANCED
SCIENCE NEWS

www.advancedsciencenews.com
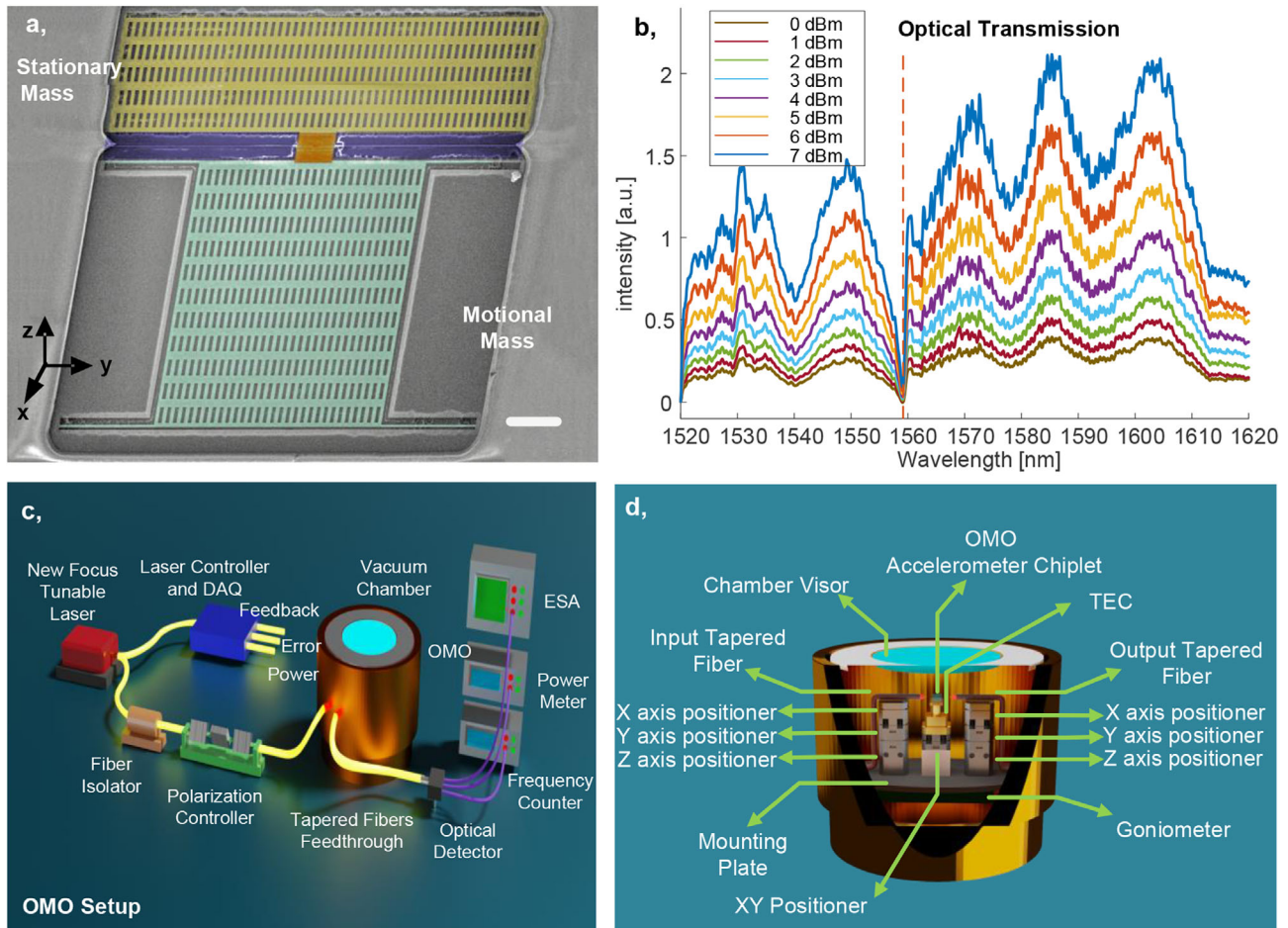
LASER
& PHOTONICS
REVIEWS

www.lpr-journal.org

Figure 1. Optomechanical inertial accelerometer: transducer and measurement setup. a) Scanning electron microscopic image of the optomechanical inertial accelerometer. The yellow-colored region represents the stationary mass and the green-colored region is the resonant mass, suspended by four cantilever beams. External force is applied in the x-axis. Scale bar = 30 μm. b) Optical transmission spectra for tuned input powers. The resonant mode (dashed vertical line) is at 1559.75 nm. c) Optomechanical oscillator (OMO) accelerometer setup. The tunable laser is connected to an optical fiber isolator and polarization controller before being fed into the vacuum chamber and coupled to the optomechanical accelerometer. The output tapered fiber is connected to the detector and the signal is analyzed on the electronic spectrum analyzer (ESA), power meter, and frequency counter. The driving laser signal is sent into the laser controller subsystem, and connected to a double feedback loop used to stabilize the laser. d) Setup within the vacuum chamber, with internal fiber positioning and drive elements for the optomechanical acceleration transduction. TEC: thermoelectric cooler. The positioner stacks are composed of an 8-axis Attocube subsystem mounted over a closed-loop goniometer, with the goniometer being capable of tilting the entire setup in order to apply varied gravitational force.

coefficient $g_{om}/2\pi$ $(= d\omega_o/dx)$.[34,35] Figure 2a shows the optomechanical transducer's characteristic mechanical frequency shift curve as a function of driving laser wavelength as it is detuned around 1559.75 nm. At the point of zero detuning ($\omega_l = \omega_c$), the characteristic slope is proportional to $g_{om}/2\pi$ and the intracavity power, as described in Section SVII (Supporting Information). The driven optical mode and the exited mechanical mode constitute a pair of linearly coupled oscillators, where the optical field is in a rotating frame. At the driving frequency, a more effective coupling between the two oscillators degenerates the effective resonant mechanical mode, and two close modes are measured.[11,36]

2.3. Optomechanical Theoretical Description

The cavity optomechanical inertial sensor can be modeled by a pair of equations of motion that are coupled together. The first

equation governs the intracavity field and transfer function of the optical resonator and the second equation models the mechanical motion. This mechanical motion can be modeled, without loss of generality, as a single degree-of-freedom damped oscillator that is driven by an optical gradient force, a thermal force, and an external force, as shown in Section SVI (Supporting Information).

If, for simplicity, we assume a system that only experiences the external applied force (F_s) defined as $F_s = ma_i$, due to acceleration along the x-axis, the mechanical equation of motion is written as

$$\ddot{x} + 2\zeta\omega_m\dot{x} + \omega_m^2 x = \frac{F_s}{m} \tag{1}$$

Here the previous relation for the damping ratio is used: $\zeta = 1/Q_m = b/2(km)^{1/2}$, where b is the damping coefficient, k is the spring constant, and $\omega_m = (k/m)^{1/2}$ is the resonant mechanical

**ADVANCED
SCIENCE NEWS**

www.advancedsciencenews.com
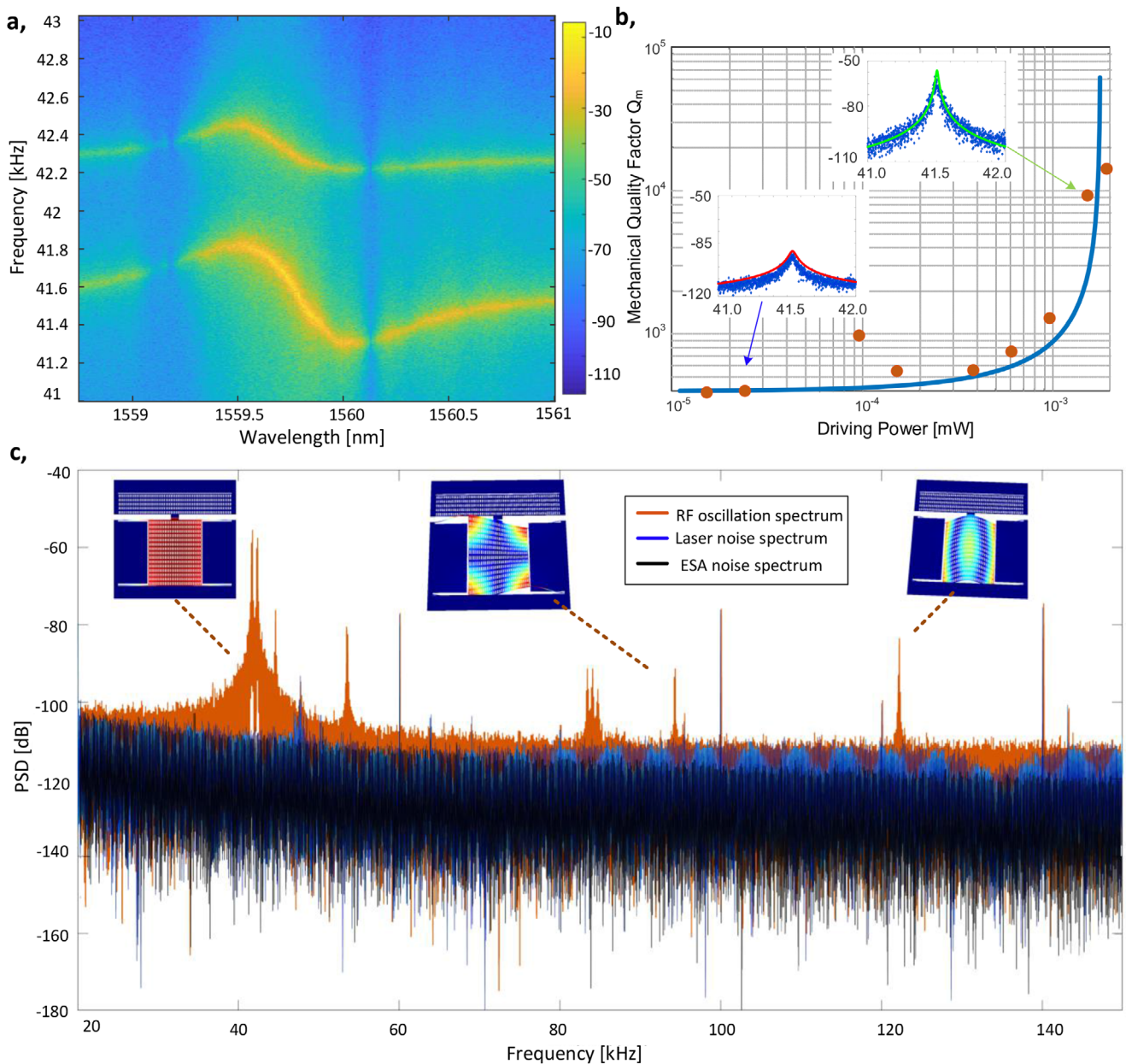
LASER
& PHOTONICS
REVIEWS

www.lpr-journal.org

Figure 2. Inertial accelerometer optomechanical stiffening, oscillation, and mode characterization. a) Parametrically driven mechanical frequency versus detuned laser drive wavelength from 1558.75 to 1561.00 nm. b) Measured mechanical quality factor (Q_m) as a function of intracavity power. Orange dots represent measured Q_m and the blue line represents the theoretical fit. As the optomechanical cavity is driven above threshold, Q_m increases exponentially. c) Transduced inertial oscillator mechanical response. Orange line represents the measured mechanical power spectral density (PSD) with a fixed pump at 1559.75 nm. The inset represents the matched mechanical eigenmodes from numerical modeling. Blue line represents the bare pump laser PSD, and the black line is the instrumentation noise floor.

frequency. When Equation (1) is solved in the Fourier domain, the relation of displacement to input acceleration is given by

$$\frac{X(\Omega)}{A_i(\Omega)} = \frac{1}{\omega_m^2 - \Omega^2 + j2\zeta\omega_m\Omega} \quad (2)$$

which shows that the dynamics of the system are determined by the frequency region of operation. In the case of resonant accelerometers, where the mechanical frequency is much higher than that of the acceleration to be detected ($\omega_m \gg \Omega$), the transfer function can be reduced to $|\frac{X(\Omega)}{A_i(\Omega)}|_{\omega_m \gg \Omega} \approx \frac{1}{\omega_m^2}$. Similarly, in the case where $\Omega \gg \omega_m$, it is $\approx \frac{1}{\Omega^2}$. From this relation, the design frequency offers a tradeoff between sensitivity and dynamic range, with a less rigid device (smaller ω_m) providing a higher sensitivity but a smaller operational frequency range.

In order to derive an equation that relates the resonant frequency shift to the applied acceleration, which causes an
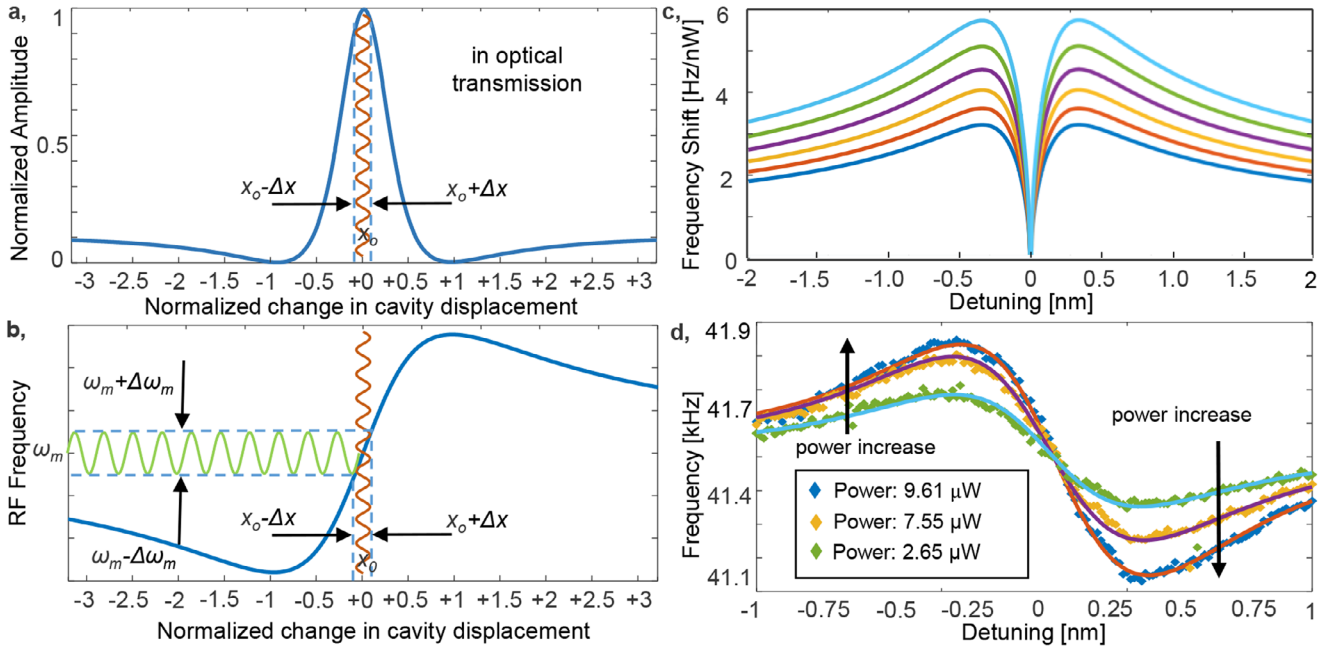
ADVANCED
SCIENCE NEWS

www.advancedsciencenews.com

LASER
& PHOTONICS
REVIEWS

www.lpr-journal.org

Figure 3. Inertial accelerometer frequency readout and power dependence. a) Normalized intracavity optical power, as a function of perturbed slot cavity displacement normalized to the transducer's maximum dynamic range. As the cavity slot width changes due to the applied acceleration or gravity, so does the intracavity power. b) Optomechanical spring effect. Subsequently as the cavity slot width changes (such as an applied acceleration in the −x-direction), the mechanical resonant frequency ω_m is perturbed by $\Delta\omega$. c) Theoretical model of perturbed frequency shift ($\Delta\omega$) as per Equation (4) with absolute frequency shift, for different drive powers of 9.82 (top curve), 7.80, 6.20, 4.92, 3.19, and 3.11 µW. A peak shift of ≈ 5.91 Hz nW^{-1} is obtained for a 0.25 nm cavity detuning from its resonant frequency. For detuning closer to the cavity resonance, a smaller frequency shift is observed. d) Measured ω_m as a function of cavity detuning for 9.61, 7.55, and 2.65 µW intracavity powers. The solid lines represent the fitted theoretical model as presented in Equation (3). Directions of change in ω_m as a function of intracavity power are presented by the arrows.

additional displacement in the slot cavity $x_s = F_s/\omega^2_m m_x$, where m_x is the effective mass, we used the coupled equations of motion for the optomechanical system, as presented in Section SVI (Supporting Information). Assuming a detuning Δ (= $\omega_l - \omega_c + g_{om}x_s$) $\gg \omega_m$, the equations can be solved,[8,27] and the effective mechanical frequency Ω_m is given by

the effective optomechanical stiffening is reduced and the effective mechanical frequency is smaller than ω_m. On the contrary, when the cavity slot width is longer than its initial resonant length ($x_o + \Delta x$), the total effective optomechanical stiffening is increased and the effective mechanical frequency is larger than ω_m. This is further represented by the orange and green curves

$$\Omega_m = \sqrt{\omega_m + \left(\frac{2|\hat{a}|^2 g_{om}^2}{\left(\left(\omega_l - \omega_c + g_{om}x_s\right)^2 + (1/2\tau)^2\right)\omega_c m_x}\right)\left(\omega_l - \omega_c + g_{om}x_s\right)} \tag{3}$$

where $|\hat{a}|^2$ is the average intracavity photon energy, g_{om} is the optomechanical coupling rate, $1/\tau = \Gamma$ is the optical cavity decay rate, ω_c is the optical resonance frequency, and ω_l is the driving optical frequency.

Equation (3) determines the effective mechanical frequency of the optomechanical accelerometer based on the device parameters and external inputs. A schematic of the optical and effective mechanical frequency variation as a function of cavity length, based on the perturbative small cavity displacements, is illustrated in **Figure 3**a,b. Here a variation on the optical cavity slot width detunes the cavity away from resonance. If the cavity slot width x_o is shorter than the original unperturbed width ($x_o - \Delta x$),

of Figure 2b, which show the effects of cavity slot width on the measured RF frequency.

In order to further examine the optical intracavity power effects on the effective mechanical frequency, the derivative of Equation (3) with respect to power is shown in Equation (4)

$$\frac{d\Omega_m}{d|\hat{a}|^2} \approx \frac{1}{2}\frac{\sqrt{\left(\frac{2g_{om}^2}{\left(\left(\omega_l-\omega_c+g_{om}x_s\right)^2+(1/2\tau)^2\right)\omega_c m_x}\right)\left(\omega_l-\omega_c+g_{om}x_s\right)}}{\sqrt{\omega_m^2+\left(\frac{2|\hat{a}|^2 g_{om}^2}{\left(\left(\omega_l-\omega_c+g_{om}x_s\right)^2+(1/2\tau)^2\right)\omega_c m_x}\right)\left(\omega_l-\omega_c+g_{om}x_s\right)}}$$

$$\tag{4}$$

The absolute value of Equation (4) versus laser-cavity detuning is shown in Figure 3c. Here the effective frequency shift, in Hz per nW of intracavity energy change, is shown for multiple driving powers: 9.82, 7.80, 6.20, 4.92, 3.91, and 3.11 μW, represented from top to bottom by the colored curves. As seen in Figure 3c, the effects over Ω_m are reduced for small detunings, and the maximum frequency shift is obtained for detunings close to ±0.25 nm. A maximum expected frequency shift of ≈ 5.91 Hz nW^{-1} is obtained when driven at 9.82 μW.

2.4. Optomechanical Sensitivity

As the specific force applied to the optomechanical accelerometer causes a change in slot cavity width Δx_s, the resonant frequency changes as described by Equation (3). At the physical level, the transducer's scale factor (S_{Fx})[37] can be defined as the ratio of change in output resonant frequency to the change in slot width due to the applied force. The equation that characterizes this shift is derived from Equation (3) as

When optically driven above threshold, the gain can exceed the mechanical resonator dissipative losses, forming an optically driven mechanical oscillator with narrow mechanical linewidths as illustrated in Figure 2b. Figure 2c shows the identified RF mechanical modes from 20 to 140 kHz, against the laser and electronic spectrum analysis noise spectrum. We observed the fundamental mechanical mode at 41.5 kHz, and the first harmonic at 83 kHz. In addition, other modes are identified through finite element simulations. Some peaks marked in orange and blue or black, correspond to detector or electronic spectrum analyzer (ESA) noise and can be subtracted from the optomechanical signal.

The theoretical fit obtained from Equation (3), modified to account for the measured optical transmission as in Figure 1b, is further compared with the measured data as seen in Figure 3d. Here the peak frequency is obtained from the electronic spectrum analyzer measurements as a function of laser detuning. Data shown in blue, yellow, and green correspond to measured data, and the curves in orange, purple, and blue correspond to

$$S_{Fx} = \frac{|\hat{a}|^2 g_{om}^3 \omega_c m_x \left(\left(\frac{1}{2\tau} \right)^2 - (\omega_l - \omega_c + g_{om} x_s)^2 \right)}{\left(\left((\omega_l - \omega_c + g_{om} x_s)^2 + (1/2\tau)^2 \right) \omega_c m_x \right)^2 \sqrt{\Omega_m^2 + \left(\frac{2|\hat{a}|^2 g_{om}^2}{\left((\omega_l - \omega_c + g_{om} x_s)^2 + (1/2\tau)^2 \right) \omega_c m_x} \right)(\omega_l - \omega_c + g_{om} x_s)}} \tag{5}$$

Furthermore, to relate this equation to the applied acceleration due to the specific force, we can use Equation (2) for the operational region where the approximation of ω_m much greater than Ω is valid. In this case, the scale factor with respect to acceleration is $S_{Fa} \approx S_{Fx}/\omega_m^2$, and the displacement can be converted to its equivalent acceleration. Equation (5) and its equivalent S_{Fa} (ratio of change in output resonant frequency to acceleration) show a change of mechanical resonant frequency in Hz/g, where g is an acceleration equal to the one produced by standard gravity $g = 9.80665$ m s^{-2}.

3. Results

3.1. Optomechanical Characterization

The measurement setup is shown in Figure 1c, with the interior details of the vacuum chamber being shown in Figure 1d. The optomechanical chiplet is placed inside the vacuum chamber and a set of Attocube stages are used to accurately position the input and output fibers as described in the "Experimental Section." An automated software controller, designed in-house for photonic chiplet testing, is used to fine-tune the coupling. In order to control the specific force to be measured, we use an Attocube ECGt5050 goniometer operating in closed-loop mode placed under the stages, inside the vacuum chamber. The chiplet is tested using changes in acceleration due to gravity inclination, which provides an accurate input when used with the closed-loop encoder and a careful map of the gravitational acceleration for the laboratory location.

the theoretical model for powers of 2.65, 7.55, and 9.61 μW. Our fit corresponds to $R^2 \approx 0.998$, and the black arrows show the direction of frequency increase. This fitting is consistent with a value of $g_{om}/2\pi = 87.74$ GHz nm^{-1}, similar to the described measurements of Section SIII (Supporting Information), done using a calibration tone.[38,39] Figure 3d shows the total peak frequency obtained from the measurements at different powers, and the model presented is in good agreement with the measured data. From these curves, there is a dependence of the mechanical resonant frequency on the intracavity power;[24,40] for example, when the cavity is pumped at high power and above the oscillation threshold, the peak mechanical frequency is also increased. This peak frequency shift can be thought of as being "accumulated" as a function of detuning, which is why the peak frequency shift in Hz nW^{-1} is at longer cavity detunings (shown earlier in Figure 3c).

Figure 4a shows the measured scale factor from our optomechanical inertial accelerometer, as well as the corresponding sensitivity. Additional information on the setup and calibration methods can be seen in Section SV (Supporting Information). The horizontal axis represents the applied acceleration in milli-g, and the vertical axis shows the change in resonant frequency from the original frequency at zero acceleration. The acceleration values are applied using the Attocube ECGt5050 goniometer, and are due to changes in gravitational acceleration in the transducer's sensitive axis. Figure 4a (inset) shows the calculated S_{Fa} from the previous equations for the measurement acceleration range. A value of 523 Hz/g is predicted and the measured value after linearization in the applied acceleration range is around 800 Hz/g.
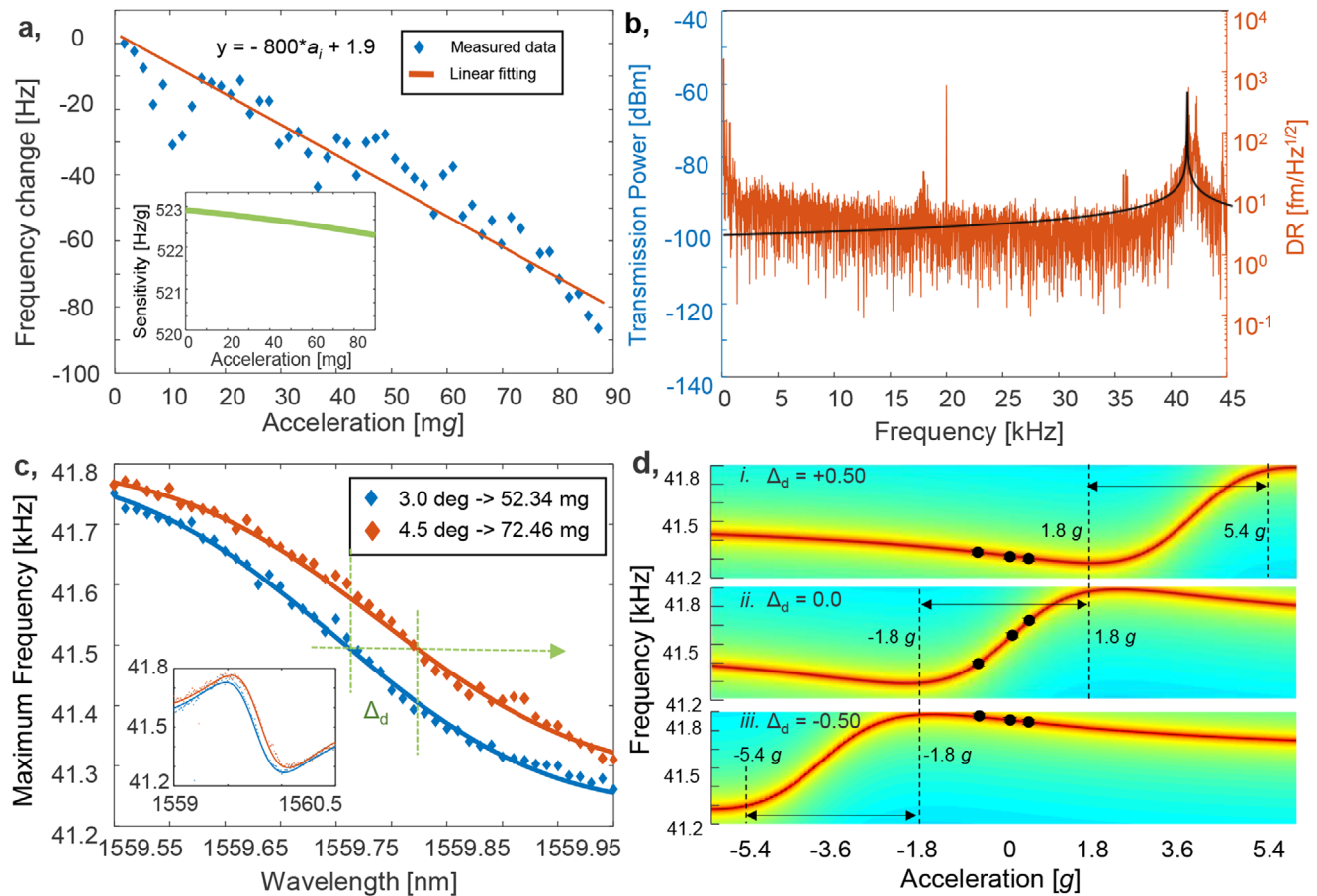
ADVANCED
SCIENCE NEWS
www.advancedsciencenews.com

LASER
& PHOTONICS
REVIEWS

www.lpr-journal.org

Figure 4. Chip-scale inertial accelerometer sensitivity and dynamic range. a) Measured resonant frequency shift as a function of applied acceleration. The applied force is tuned by the tilt angle with an Attocube ECGt5050 goniometer, in steps of 100 millideg, which corresponds to a maximum applied acceleration of ≈87 mg. The inset shows the corresponding measured sensitivity—equivalently the scale factor—versus acceleration as obtained from Equation 5. b) Measured transmission PSD and corresponding displacement resolution from the test optomechanical inertial accelerometer. The left axis shows the measured spectral power as measured from the ESA, and the right axis shows the corresponding displacement resolution converted from the signal transmission PSD. The low-frequency noise is due to the spectrum analyzer instrument dynamic range and resolution bandwidth limit. The peaks at ≈20 kHz are from laser and detector noises. The black curve represents the theoretical fit of the fundamental frequency. A measured displacement resolution of ≈2.5 fm Hz$^{-1/2}$ is obtained, which corresponds to a force-equivalent acceleration of 17.02 µg Hz$^{-1/2}$. c) Measured maximum frequency as a function of driving wavelength for different input accelerations (blue is for 3.0° inclination (52.34 mg); orange is for 4.5° inclination (72.46 mg)). The superimposed curves in blue and orange represent the theoretical fit using Equation (3). The inset shows the complete 2D sweep. As it can be seen from the green arrows, as acceleration is applied to the optomechanical device, there is a redshift in the optical resonant frequency $\Delta\omega_o$, with the entire 2D sweep redshifted, as a function of increasing cavity displacement x_s. d) Dynamic range extension demonstration: i–iii) a set of similar optomechanical accelerometers with the same design, sensitivity, and dynamic range. Device (ii) is set to measure a range of accelerations from $-1.8g$ to $+1.8g$. Devices (i) and (iii) are being driven at a detuned wavelength and are not affected by the optomechanical stiffening until a sufficiently large magnitude acceleration induces a detectable displacement x_s. With the large magnitude acceleration, the detuning is in the sensitive optomechanical sensing regime for devices (i) and (iii), enabling the measurements of accelerations from $+1.8g$ to $+5.4g$ in device (i), and from $-5.4g$ to $-1.8g$ in device (iii).

In addition to the scale factor calculations, Figure 4b shows the PSD of the optomechanical accelerometer for frequencies between DC and 45 kHz, with the cavity being driven at 9.61 µW, as characterized above. The signal was measured using a Keysight N9010A EXA singnal analyzer with a bandwidth from 10 Hz to 26.5 GHz. The additional low-frequency noise observed is due to the instrument dynamic range and resolution bandwidth limit. In order to convert PSD into DR, we use the transmitted optical component that has been modulated by the mechanical motion of the resonant mass. This is done by normalizing the optical transmission shown in Figure 1b and the power that reaches

the optical detector.[8] As it can be seen from Figure 4b (right axis), the obtained displacement noise floor is ≈ 2.5 fm Hz$^{-1/2}$, which corresponds to an equivalent force acceleration of 17.02 µg Hz$^{-1/2}$.

3.2. Extended Dynamic Range and Tradeoffs

An often tradeoff in accelerometer implementation is between dynamic range and scale factor (sensitivity). An inertial accelerometer that is designed with a softer flexure would yield a

higher mechanical displacement, translating into a larger scale factor, and larger mechanical frequency shift per unit of applied acceleration. However, large nonperturbative displacements typically cannot be measured due to limitations in sensor linearity, limiting the dynamic range.

To overcome this, force rebalance and other techniques to offset the transducer have been successfully used to extend the inertial accelerometer dynamic range.[41–43] While offset approaches would shift the dynamic range, force rebalance still suffers from the described tradeoff: at its core, the rigidity of the sensing element is increased (such as by applying an electric charge) yielding a smaller transducer scale factor while operating over a larger range of accelerations. Furthermore, the additional control loop required to fine-tune the electrostatic force introduces extra measurement noise and is a source of scale factor nonlinearity.

In contrast to prior force rebalance, our optomechanical accelerometer can be configured for an extended dynamic range operation, while retaining the superior scale factor from the original design. This dynamic range extension approach is depicted in Figure 4d-i–iii, which shows the resulting mechanical resonant frequency from Equation (3) for different operating laser-cavity detunings. In subpanel (ii), the optomechanical transducer is first driven at an optical wavelength ω_d, and has a dynamic range that spans from $-1.8g$ to $+1.8g$, producing the resonant frequency ($\omega_m/2\pi$) versus input acceleration curve depicted in red. Subsequently our inertial accelerometer is driven at a detuned wavelength of $\omega_d + 0.5$ nm as shown in subpanel (i); the entire acceleration response curve is now shifted to the right, and the sensor operates for range of applied accelerations from $+1.8g$ to $+5.4g$. A similar effect is obtained if the transducer is now driven at a wavelength of $\omega_d = -0.5$ as in subpanel (iii), where the measurement range becomes $-1.8g$ to $-5.4g$. At the physical level, the extension of the sensor's dynamic range is related to the optical cavity resonant mode. Particularly, when a specific force changes the slot width of the optical cavity, the optical resonant frequency ω_c also changes and the characterization curve shifts. Applying an optical driving wavelength detuned with a positive Δ_d to the cavity means that the system will enter in resonance with the driving wavelength only when the cavity slot width is increased (with the acceleration and force-induced displacement) to the optimal optomechanical stiffening–softening points ($\approx 4g$ for subpanel (i)). This enables the single inertial transducer to sense accelerations in different ranges while maintaining the sensitivity and scale factors.

Figure 4c shows the described technique for experimental data measured from the optomechanical transducer. The inset shows the total characteristic curve of resonant mechanical frequency as a function of driving wavelength when different accelerations are applied by using the goniometer. These curves are magnified in the main figure. The points in blue represent the measured data when an inclination of 3.0° was applied to the accelerometer which is equivalent to an acceleration of 52.34 mg; similarly, the points in orange are taken at 4.5° inclination or 72.46 mg. Both sets of data have been fitted by using Equation (3), presented by the blue and orange curves. The green lines represent the operational frequency change of the optomechanical accelerometer with the applied accelerations. In addition, Figure 4d shows the dynamic range extension configuration derived from the measured data on Figure 4c, where the back figures have been derived

by using Equation (3) and the parameters obtained from the fittings of Figure 3d and Section SVII (Supporting Information), as previously described in this section. For the demonstrated configuration, a three-sensor array operating at a 0.5 nm detuning step size is shown as a function of the applied acceleration on the chiplet. The center chiplet in subpanel (ii) is set to measure accelerations in the range from -1.8g to +1.8g. When the other cavities are operated at a wavelength greatly detuned from resonance (in this case, 0.5 nm), these cavities are taken out of the main optomechanical resonance and are not affected by optical stiffening in the same way as the first device. However, these cavities can get into resonance again when the right acceleration is applied to them, and the cavity width becomes longer or shorter depending on the detuning direction. The main reason that makes the dynamic range extension possible is that by having a 7.2 ng mass, the optomechanical accelerometer's cavity displacement ranges in the approximately femtometer level for the smaller detectable accelerations, and in the ≈250 pm level for top accelerations inside the operating dynamic range, meaning that the mechanical system has not reached its nonlinear region, and there is plenty of room for further operation. As it can be seen, the transducer on subpanel (i) becomes active for accelerations from +1.8g to +5.4g and device (iii) from $-5.4g$ to $-1.8g$. The shown data points on the theoretical curves show measured frequency as a function of applied acceleration for the three configurations described. As it can be seen, theoretical frequency estimates match the obtained data, and the dynamic range on the system is effectively multiplied by the number of sensors in the array, in this case by three times. Since the optomechanical transduction is maintained, operation on this detuned region does not affect the measured sensitivity, and mechanical frequency changes due to optical gradient force are obtained in the new operational regions. Other configurations to further extend the dynamic range with more optomechanical transducers can also be assembled.

4. Conclusion

In this study, we have presented a theoretical derivation of the equations of sensitivity and peak frequency change for an optomechanical accelerometer used in frequency readout mode. The model was evaluated by matching data measured from a device nanofabricated in 250 nm silicon-on-insulator (SOI). And we have demonstrated a 1.5 mg Hz^{-1} sensitivity, a 2.5 fm Hz$^{-1/2}$ displacement resolution, with a 5.91 Hz nW^{-1} power sensitivity, and a 17.02 μg Hz$^{-1/2}$ force-equivalent acceleration. Our inertial accelerometer is integrated on-chip, enabled for packaging, with a laser-detuning-enabled approach for dynamic range extension while maintaining the precision sensing sensitivity.

5. Experimental Section

Device Nanofabrication: The optomechanical accelerometers were fabricated both at the complementary metal-oxide semiconductor (CMOS) foundry in the Institute of Microelectronics, Singapore and at the University of California Los Angeles, Nanofabrication Laboratory (NanoLab) in Los Angeles, CA, USA. The initial substrate was a SOI wafer that had a 250 nm top silicon layer, and a 3 μm thermal oxide buried cladding. The photonic crystal was first fabricated by using a 248 nm deep ultraviolet (DUV) lithography stepper in two different processes, which is

also described in ref. [44]. A first sacrificial oxide layer was used to pattern the 100 nm slot line width by using residual slope in the oxide etch. Afterward, the bottom oxide was etched with tight process control, and served as a mask to etch the silicon layer. In the next steps, the 185 nm photonic crystal holes were etched by using reactive ion etching (RIE). Finally, a third silicon etching process was used to fabricate the 7.2 ng mass as well as the other larger features larger than 1 μm. Numerous variants of self-consistent dose correction were applied to correct proximity effects. In order to release the optomechanical accelerometer and overcome stiction, a three-step lithography process was used. Two different positive masks were used to protect the cladding of the integrated waveguides, during a time-controlled etching process designed to expose the top silicon layer. Finally, a third negative mask was used for the final release and undercut of the movable structures. The nanocavities were air-bridged via wet etching by using a 6:1 buffered-oxide etchant for 20 min, followed by an overnight photoresist stripper process. The resultant structures were dried on a Tousimis critical point dryer by using low filling rate and a longer purge time, appropriate for delicate samples. The result of the process provided improved yield and coupling efficiency.

Experiment Setup: The optomechanical accelerometer was mounted inside a Janis ST-500 vacuum chamber, as shown in Figure 1d. The chiplet was set in a center stage with Attocube positioners that can move it in the x–y direction, and a temperature controller with 10 mK accuracy. A pair of lensed fibers were mounted each on one side of the chiplet, as shown, and each of the fibers were setup on top of a 3-axis Attocube stack that can fine tune the position of the fiber in the x-, y-, and z-directions. The chosen optical fibers had antireflective (AR) coating and were operated at a working distance of 12 μm. These components were mounted on a custom-made plate, designed to fit on top of an ECGt5050 goniometer, which was placed inside the vacuum setup and was capable of tilting the chiplet in order to apply a constant specific force to the transducer. The change in specific force was accurately known by using a gravitational model for the location of the laboratory at UCLA and calculated by using the tilt values obtained from the encoder in the goniometer. The goniometer was operated in closed loop mode and had a resolution of 1 μdeg.

On top of the setup, an automated microscope and camera were mounted to monitor the setup. The 8-axis Attocube stacks are controlled using a custom-made LabView virtual instrument program that integrates the piezocontroller drivers with the microscope controllers and the measurement instruments. The software is capable of automatically coupling the tapered lensed fiber to the inverse couplets from the chiplets, and optimizing the transmission power. The software is designed to take measurement data from the experiment and save them according to the type of data collected and the instrument used.

The instruments which were connected to the vacuum chamber are shown in Figure 1c. A New Focus Velocity tunable laser was used in order to provide the driving power to the optomechanical accelerometer, and the operating wavelength was carefully set after the cavity was characterized for an initial optical resonance detuning as explained in the "Results" section. The optical power was split with a 90/10 fiber splitter. The first arm was sent into a fiber isolator and to an automatic polarization controller that was operated by using the LabView automated software. After this, the optical fiber was fed into the vacuum chamber. The second arm was used to monitor the initial transmission power, and went to an external setup that feedbacks to the New Focus Laser. Finally, the transmission spectrum was monitored with a balanced detector. The output signal was split to a power meter, a reciprocal frequency counter, and an Agilent N9010A EXA signal analyzer.

Numerical Modeling: The optomechanical accelerometer model presented was obtained by solving the coupled equations of motion in terms of Bessel functions. This equation was approximated for the operational point using the conditions described in Section SVII (Supporting Information), and described the optical stiffening interaction due to oscillator dynamics. The photonic crystal was first modeled by using COMSOL Multiphysics, where the first two optical modes were calculated and optimized for small wavelength confinement. In a similar way, the mechanical mass was studied in COMSOL, where the permitted modes of oscillation for the structure were calculated as presented in Figure 2c.

Conflict of Interest

The authors declare no conflict of interest.

Data Availability Statement

The data that support the findings of this study are available from the corresponding author upon reasonable request.

[1] B. Abbott, R. Abbott, T. D. Abbott, M. Abernathy, F. Acernese, K. Ackley, LIGO Scientific Collaboration and Virgo Collaboration, *Phys. Rev. Lett.* **2016**, *116*, 061102.

[2] Y. Ekim, J. Carballo, K. Takeda, *IEEE Access* **2020**, *8*, 58443958469.

[3] D. Israel, K. Mauldin, C. Roberts, J. Mitchell, A. Pilkkinen, L. V. Cooper, M. Johnson, S. Christe, C. Gramling, in *2020 IEEE Aerospace Conf.*, Big Sky, MT **2020**, up pp. 1–14.

[4] Y. Wang, H. Ding, X. Le, W. Wang, J. Xie, *Sens. Actuators, A* **2017**, *254*, 126.

[5] S. Shin, A. Daruwalla, M. Gong, A. Wen, F. Ayazi, in *2019 20th Int. Conf. on Solid-State Sensors, Actuators and Microsystems*, Berlin, Germany, **2019**, pp. 503–506.

[6] C. Wang, F. Chen, Y. Wang, S. Sadeghpour, C. Wang, M. Baijot, R. Esteves, C. Zhao, J. Bai, H. Liu, M. Kraft, *Sensors* **2020**, *20*, 4054.

[7] A. Shkel, in *IEEESensors*, **2010**, pp. 5–9.

[8] Y. Huang, J. G. Flor Flores, Y. Li, W. Wang, D. Wang, N. Goldberg, J. Zheng, M. Yu, M. Lu, M. Kutzer, D. Rogers, D. Kwong, L. Churchill, C. W. Wong, *Laser Photonics Rev.* **2020**, *14*, 1800329.

[9] G. Anetsberger, E. Gavartin, O. Arcizet, Q. Unterreithmeier, E. M. Weig, M. L. Gorodetsky, J. P. Kotthaus, T. J. Kippenberg, *Phys. Rev. A* **2010**, *82*, 061804.

[10] G. Fedder, C. Hierold, J. Korvink, O. Tabata, *Resonant MEMS: Fundamentals, Implementation, and Application*, John Wiley & Sons, Weinheim, Germany **2015**.

[11] A. Krause, M. Winger, T. Blasius, Q. Lin, O. Painter, *Nat. Photonics* **2012**, *6*, 768.

[12] Y. L. Li, P. F. Barker, *J. Lightwave Technol.* **2018**, *36*, 3919.

[13] B.-B. Li, L. Ou, Y. Lei, Y.-C. Liu, *Nanophotonics* **2021**, *10*, 2799.

[14] A. A. Clerk, M. Devoret, S. Girvin, F. Marquardt, R. Schoelkopf, *Rev. Mod. Phys.* **2010**, *82*, 1155.

[15] S. Schreppler, N. Spethmann, N. Brahms, T. Botter, M. Barrios, D. Stamper-Kurn, *Science* **2014**, *344*, 1486.

[16] R. Hopkins, J. Miola, W. Sawyer, R. Setterlund, B. Dow, in *Proc. of the 2005 National Technical Meeting of the Institute of Navigation*, San Diego, CA **2005**, pp. 970–979.

[17] J. Zhang, Y. Su, Q. Shi, A.-P. Qiu, *Sensors* **2015**, *15*, 30293.

[18] Z. Yang, J. Zhao, X. Wang, G. Xia, A. P. Qiu, Y. Su, Y. P. Xu, *IEEE J. Solid-State Circuits* **2015**, *50*, 2113.

[19] X. L. Feng, C. J. White, A. Hajimiri, M. Roukes, *Nat. Nanotechnol.* **2008**, *3*, 342.

[20] D. B. Leeson, *Proc. IEEE* **1966**, *54*, 329.

[21] T. Lee, A. Hajimiri, *IEEE J. Solid-State Circuits* **2000**, *35*, 326.

[22] E. Rubiola, *Phase Noise and Frequency Stability in Oscillators*, Cambridge University Press, Cambridge **2008**.

[23] J. Manley, D. Chowdhury, D. Grin, S. Singh, D. Wilson, *Phys. Rev. Lett.* **2021**, *126*, 061301.

[24] Y. Huang, J. G. Flor Flores, Z. Cai, J. Wu, M. Yu, D.-L. Kwong, G. Wen, L. Churchill, C. W. Wong, *Opt. Express* **2017**, *25*, 6851.

[25] Y. Huang, J. G. Flor Flores, Z. Cai, M. Yu, D.-L. Kwong, G. Wen, L. Chruchill, C. W. Wong, *Sci. Rep.* **2017**, *7*, 4383.

[26] Y. Huang, J. Wu, J. G. Flor Flores, M. Yu, D.-L. Kwong, G. Wen, C. W. Wong, *Appl. Phys. Lett.* **2017**, *110*, 111107.

[27] Y. Li, J. Zheng, J. Gao, J. Shu, M. Aras, C. W. Wong, *Opt. Express* **2010**, *18*, 23844.

[28] Y. Akahane, T. Asano, B.-S. Song, S. Noda, *Opt. Express* **2005**, *13*, 1202.

[29] J. Gao, J. McMillan, M. C. Wu, J. Zheng, S. Assefa, C. W. Wong, *Appl. Phys. Lett.* **2010**, *96*, 051123.

[30] M. Hossein-Zadeh, K. Vahala, *Opt. Lett.* **2007**, *23*, 1611.

[31] B. Sheard, M. Gray, C. Mow-Lowry, D. McClelland, S. Whitcomb, *Phys. Rev. A* **2004**, *69*, 051801.

[32] H. Rokhsari, T. Kippenberg, T. Carmon, K. Vahala, *IEEE J. Sel. Top. Quantum Electron.* **2006**, *12*, 96.

[33] J. G. Flor Flores, W. Wang, Y. Huang, J. Wu, T. Yerebakan, Q. Bai, C. W. Wong, in *2020 Conf. on Lasers and Electro-Optics (CLEO)*, San Jose, CA **2020**, pp. 1–2.

[34] M. Wu, A. Hryciw, C. Healey, D. Lake, H. Jayakumar, M. Freeman, J. Davis, P. Barclay, *Phys. Rev. X* **2014**, *4*, 021052.

[35] T. Kippenberg, H. Rokhsari, T. Carmon, A. Scherer, K. Vahala, *Phys. Rev. Lett.* **2005**, *95*, 033901.

[36] W. Bowen, G. Milburn, *Quantum Optomechanics*, CRC Press, Boca Raton, FL **2016**.

[37] IEEE Aerospace and Electronic Systems Society, *IEEE Standard for Inertial Sensor Terminology, IEEE Std 528-2001*, IEEE, New York, NY **2001**.

[38] M. Gorodetksy, A. Schliesser, G. Anetsberger, S. Deleglise, T. Kippenberg, *Opt. Express* **2010**, *18*, 23236.

[39] K. Schneider, Y. Baumgartner, S. Hönl, P. Welter, H. Hahn, D. Wilson, L. Czornomaz, P. Seidler, *Optica* **2019**, *6*, 577.

[40] J. G. Flor Flores, Y. Huang, L. Li, V. Iaia, M. Yu, D.-L. Knowng, C. W. Wong, in *Conf. on Lasers and Electro-Optics (CLEO), San Jose, CA 2017, SF2I.6*.

[41] S. Yan, Y. Xie, M. Zhang, Z. Deng, L. T. Tu, *Sensors* **2017**, *17*, 2669.

[42] X. Huang, Z. Deng, Y. Xie, Z. Li, J. Fan, L. Tu, *Sensors* **2017**, *17*, 2471.

[43] K. H.-L. Chau, S. R. Lewis, Y. Zhao, R. T. Howe, S. F. Bart, R. G. Marcheselli, *Sens. Actuators, A* **1996**, *54*, 472.

[44] X. Luan, Y. Huang, Y. Li, J. F. McMillan, J. Zheng, S.-W. Huang, P.-C. Hsieh, T. Gu, D. Wang, A. Hati, D. A. Howe, G. Wen, M. Yu, G. Lo, D.-L. Kwong, C. W. Wong, *Sci. Rep.* **2014**, *4*, 6842.